Ballistic performance of porous-ceramic, thermal protection systems to 9 km/s

Joshua E. Miller[1] and William E. Bohl[2]
Lockheed Martin Space Systems Company, Denver, CO, 80127

Cory D. Foreman[3]
Lockheed Martin Exploration and Science, Houston, TX, 77058

and

Eric C. Christiansen[4] and Bruce A. Davis[5]
NASA Johnson Space Center, Houston, TX 77058

Porous-ceramic, thermal protection systems are used heavily in current reentry vehicles like the Orbiter, and they are currently being proposed for the next generation of US manned spacecraft, Orion. These materials insulate the structural components and sensitive components of a spacecraft against the intense thermal environments of atmospheric reentry. These materials are also highly exposed to solid particle space environment hazards. This paper discusses recent impact testing up to 9.65 km/s on ceramic tiles similar to those used on the Orbiter. These tiles are a porous-ceramic insulator of nominally 8 lb/ft^3 alumina-fiber-enhanced-thermal-barrier (AETB8) coated with a damage-resistant, toughened-unipiece-fibrous-insulation/reaction-cured-glass layer (TUFI/RCG).

Nomenclature

A = piston area
F_H = hydrodynamic force
F_M = mechanical force
M = accumulated piston mass
$\overline{m_p}$ = equivalent areal density of the projectile
$\overline{m_T}$ = TUFI/RCG layer areal density
r_p = projectile initial radius
s = proportionality constant for shock wave velocity to piston velocity for tile
s_T = proportionality constant for shock wave velocity to piston velocity for TUFI/RCG layer
U = shock wave front velocity
U_i = impact velocity
U_m = mean fragmentation/melt velocity
U_0 = initial shock wave front velocity in the tile
Y_0 = tile compression strength
x = position
x_f = position at zero velocity ratio
ρ_0 = tile density
ρ_p = projectile density
ω = expansion ratio (lateral velocity to axial shock wave velocity)

---

[1] Sr. Mechanical Engineer, Nonlinear Flight Analysis, PO Box 179/W3004, and AIAA Professional.
[2] Sr. Staff Mechanical Engineer, Nonlinear Flight Analysis, and PO Box 179/W3004.
[3] Systems Engineer, Specialty Engineering, and 2625 Bay Area Boulevard/A7A.
[4] Insert Job Title, Department Name, Address/Mail Stop, and AIAA Member Grade for fourth author.
[5] Insert Job Title, Department Name, Address/Mail Stop, and AIAA Member Grade for fifth author.

I. Introduction

POROUS-CERAMIC tiles insulate atmospheric reentry vehicles from intense heat of the reentry plasmas generated by atmospheric braking of the spacecraft from orbital velocities. Due to the necessity that these materials create a temperature gradient of approximately a thousand Kelvin over their thickness, it is important that the material is as near the prescribed values prior to reentry as possible. However, these tiles are also in general on exposed surfaces to environmental threats like meteoroids and orbital debris leaving a probability that these exposed surfaces will be below their prescribed values. Owing to the typical small size of impact craters into these materials, the local flow fields over these craters afford some margin in thermal protection designs for these locally reduced performance values.

The acceptability of a locally reduced thermal protection system is limited, however, with the key limit being a direct impingement of the reentry plasma on spacecraft structure. For regions of the vehicle that are subjected to the most intense reentry environments, this limit of acceptability can also be realized even if the structure is not directly exposed. For these cases the flow field ingests enough energy into the plasma within the cavity, that a sufficiently high temperature is achieved to generate thermal gradients that heat structural elements above their safe operating condition despite the presence of residual thermal-protection material. The remaining thickness of insulating material after an impact is then an important parameter describing the worthiness of the vehicle to reenter. As such, the depth of penetration is the principal observable required when testing the performance of these materials to the meteoroid and orbital debris environment. In the testing reported here, these materials have been impacted with projectiles typical of the orbital debris and meteoroid environments [3] to determine the depth of penetration.

Tests reported herein have been performed at NASA's White Sands Test Facility's two-stage gas guns to $\gtrsim$ 8 km/s and at University of Dayton Research Institute's two- and three-stage gas guns to $\gtrsim$ 9 km/s. Both facilities are capable of precision measurements of pre-test projectiles, impact velocities to ±0.2 km/s and projectile integrity verification prior to impact. Post-test damage measurements are taken by Johnson Space Center's Hypervelocity Impact Test Facility personnel and volumetric measurements taken by Kennedy and Johnson Space Center non-destructive evaluation personnel.

II. Tile Impact Tests

The tests performed are on target thermal protection materials typical of those described in Rasky, et al. [1] and illustrated in Figure 1. The materials represented from right to left in Figure 1a are a spherical projectile impacting a tile with a thin toughened-unipiece-fibrous-insulation/reaction-cured-glass (TUFI/RCG) layer on the external surface. The TUFI/RCG layer is a thin layer that goes approximately from the density of amorphous silica to the tile density. Opposite the TUFI/RCG layer is another densification layer that provides a bonding surface for the bonding agent to attach the tile to the structural panel. In Figure 1b, a density profile from right to left shows the high density TUFI/RCG layer which tapers to the density of tile with its rear densification layer and the bonding pad and substrate to the extreme left.

The TUFI/RCG layer provides both handling and water proofing benefits, but it also provides a relatively high shock wave impedance material to push impacting materials to a higher pressure on impact resulting in increased fragmentation and/or melt of the threat particle, which in turn decreases threat potential. Upon entering the relatively low tile density, the shock wave compressed impacting material decompresses as it propagates resulting in the scattering of fragments and diffusion of molten or gaseous material. For threat particles too big to be arrested in the tile material, the densification and bonding layers' increased density provides an increasing arresting potential prior to material impact on the structural panel.

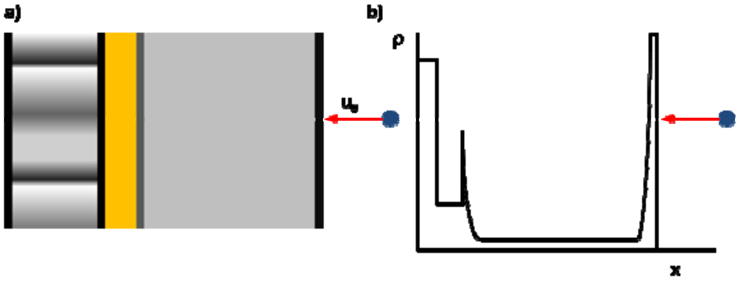

Figure 1. (a) Target layout and (b) density profile to structural panel.

In Fig. 2, a pair of orthogonal views of a titanium powder enhanced X-ray image of a test article is shown for an off-normal tile impact along with its damage measurements. The uppermost high-contrast plane in the views is the TUFI/RCG layer and the lowermost is the densification layer. The damage measurement normal to the TUFI/RCG layer is the maximum depth of penetration and the damage measurement parallel to the TUFI/RCG layer is the width. The product of the identified maximum depth of penetration and the tile density is the penetrated areal density value which can be used with the areal densities of the various layers of the thermal protection system.

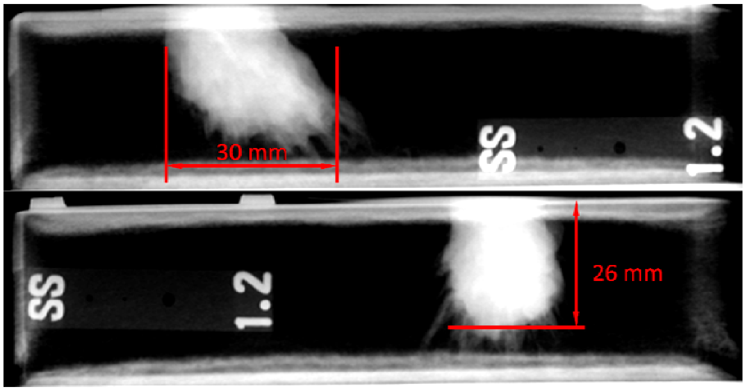

Figure 2. Titanium-powder-enhanced, orthogonal views and measurements of an impact crater for an off-normal impact.

This effort has performed 26 shots where the main projectile cavity is within the tile and minimal bonding pad damage has occurred. The findings of a subsection of these shots that do not include tile edge or substrate facesheet effects are summarized in Table 1. Through the course of these shots the projectile materials considered have been Nylon™ (1.14 g/cm^3), aluminum (2.796 g/cm^3) and steel (7.68 g/cm^3) with the bulk of the tests using aluminum projectiles. The penetrated cavity depth and width are recorded for a variety of projectile sizes, impact angles ranging from impacts normal to the target surface to 60°, and impact speeds ranging from 4 to 9 km/s. For the normal impact cases, the width of the cavity corresponds to the diameter of the cavity. Along with the variable impact conditions, two areal densities of TUFI/RCG, 0.209±0.012 and 0.158±0.009 g/cm^2, have been considered.

The dependence of the projectile mass on the parameters identified in Table 1 is shown in Figure 4. As can be seen in this figure, the dependence of the critical projectile mass is approximately proportional to the fourth power

Table 1. Summary of test results including the areal density of the TUFI/RCG layer in the test, the diameter and density of the projectile, the impact speed and obliquity, and the penetrated depth and cavity width.

HITF #	*TUFI/RCG (g/cm^2)*	*Diameter (mm)*	*Density (g/cm^3)*	*Speed (km/s)*	*Obliquity (°)*	*Depth (cm)*	*Width (cm)*
7468	0.209	1.0	2.796	7.04	0	1.10	0.90
9234	0.158	1.0	2.796	7.24	0	1.45	1.05
8297	0.209	1.0	2.796	7.88	0	1.10	0.95
9252	0.158	1.0	2.796	8.28	0	1.40	1.10
9253	0.158	1.6	1.14	8.17	0	1.50	1.40
9313	0.209	1.6	2.796	9.65	0	2.50	2.00
9308	0.158	1.6	2.796	9.26	0	2.75	1.70
8313	0.209	1.6	2.796	9.13	0	2.20	1.70
9435	0.158	1.3	7.68	4.08	0	3.30*	0.60
9434	0.158	1.3	7.68	7.10	0	3.50*	0.80
9271	0.158	2.0	2.796	4.16	0	2.80*	1.15
9235	0.158	2.0	2.796	7.19	0	3.40	1.55
7469	0.209	2.4	2.796	7.00	0	3.85*	1.85
9314	0.209	2.6	2.796	9.18	0	4.40	2.30
9238	0.158	2.8	1.14	7.12	30	2.45	2.50
9250	0.158	3.2	1.14	6.87	30	2.85	2.60
7472	0.209	3.2	1.14	7.15	30	2.80	3.10
9236	0.158	2.0	2.796	4.39	45	1.90	2.20
9240	0.158	2.0	2.796	7.06	45	2.30	2.50
9309	0.158	2.1	2.796	9.47	45	2.75	3.10
9312	0.158	3.2	1.14	9.36	45	2.80	3.60
7470	0.209	3.0	2.796	4.20	45	2.80	3.25
9245	0.158	3.0	2.796	4.13	45	3.30	3.50
7473	0.209	1.6	7.68	6.95	60	2.10	2.45
9310	0.158	2.6	2.796	9.15	60	2.80	3.10
7471	0.209	3.0	2.796	6.97	60	2.60	3.65
9237	0.158	3.0	2.796	6.85	60	2.90	3.00
9277	0.158	3.4	2.796	6.89	60	3.40	4.00

* Equivalent penetration depth due to penetration into the densification layer

of the penetrated areal density (the total of the TUFI/RCG areal density and product of the tile density and penetration depth from Table 1) and inversely proportional to the areal density of the TUFI/RCG layer alone, the density of the projectile to the one-third power, the normal component of velocity and an additional cosine of the impact angle. Therefore, adding additional areal density to the coatings of a the tile increases the size of a projectile that can be arrested, but it is more efficient to increase the thickness of the tile than the areal density of the TUFI/RCG assuming the TUFI/RCG is sufficient for the threat particle. It is also noteworthy that while many of these exponents are similar to those found in [4], the exponent of velocity indicates a scaling on momentum rather than kinetic energy. The principal difference in the targets used here in comparison with those of [4] is the TUFI/RCG layer, where the former only had an outer densification layer of about 0.04 g/cm^2 in contrast to these targets that have approximately 4 to 5 times the added mass per unit area.

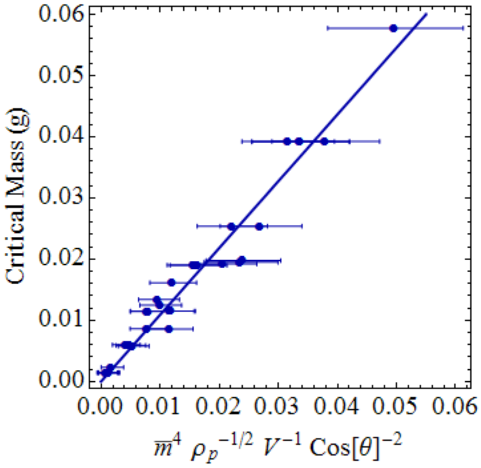

Figure 4. Critical mass dependence on impact parameters.

Enhanced X-ray images of normal impact cavities that resulted from aluminum projectiles with diameters of 1 mm (left) and 2.4 mm (center) aluminum projectiles at ~7 km/s and a 1.6 mm aluminum projectile at ~9 km/s are shown in Figure 3. The 7 km/s impacts have damage cavities that are about one to one for the 1 mm projectile and five-thirds to one times for the 2.4 mm projectile, while the 9 km/s impact damage cavity is also very nearly one to one. Consequently, the damage profile is not just a function of projectile, but also a function of impact velocity. Additionally the deepest fragments in the 1 mm and 7 km/s and 1.6 mm and 9 km/s impacts hold to the penetration depth being about five-thirds of the cavity diameter. Another effect of velocity is illustrated in Figure 5 where the average dependence on areal density from the normal impacts with aluminum projectiles as shown in Figure 4 is used to normalize the projectile masses. As can be seen the critical projectile size decreases approximately linearly as the impact speed moves from 4 to 7 km/s, but approximately increases beyond 7 km/s to 9 km/s.

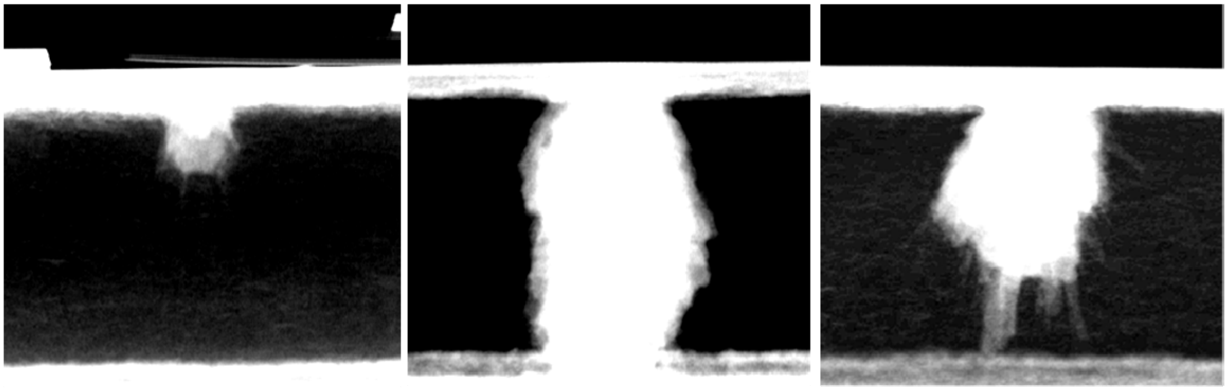

Figure 3. Cavity size dependence on target and impact characteristics for a small projectile and large projectile at 7 km/s and a intermediate projectile at 9 km/s.

III. Test Results Discussion

As mentioned, one of the key differences between the tiles of [4] and this work is the 4 to 5 times thicker TUFI/RCG layer. This layer is used to facilitate the fragmentation or vaporization of the projectile prior to entering the low density tile material; however, after the projectile passes through the TUFI/RCG layer, the projectile is not generally completely converted to fragments of sufficiently small size to erode away while passing through the tile material. This failure to vaporize is especially true for TUFI/RCG layers that are too thin for a projectile with a binding energy much higher than the energy behind the shock wave front. For these solid fragments the remnants propagate through the tile leaving deep penetrations until their kinetic energy is dissipated with very small cavity radius to depth ratio (ω) cavities. Energy deposition into highly compressible materials similar to tiles, like gases and aerogels, have been considered by multiple researchers due to both the use of hypersonic projectiles, interest in meteor entrance in both atmospheres and aerogels [5-8]. With regard to atmospheric reentry, these small ω penetrations are highly choked and do not ingest flow very well, and as such, are assumed to be inconsequential as long as structural integrity is not compromised.

The vaporized material, on the other hand, leaves ω ratios near a half, and as a consequence the cavities that result from vaporization are very much of interest to flow ingestion on reentry. Owing to the vaporization and fragmentation, it is necessary to reconsider the models developed in [5-8] to describe the penetration mechanics and extend them to a radially expanding debris cloud that results from a nearly discrete interaction with the TUFI/RCG layer.

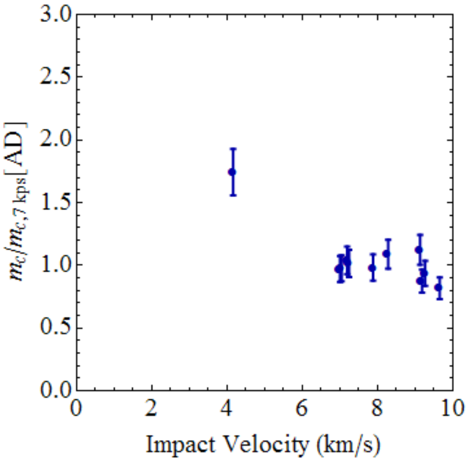

Figure 5. Normalized critical mass as a function of velocity for normal aluminum impacts

It has been observed that porous materials, after passage of a strong shock wave, jump to about the density of the crystalline material, or put differently, the jump conditions populate an isochor near the crystalline material density. This property of a shock wave manifests in a linear relationship between the shock wave velocity and the particle velocity without a constant offset or $U = s\,u_p$ where U, u_p and s are the shock wave velocity, the particle velocity and proportionality constant, respectively. The hydrodynamic force, F_H, experienced by the impacting particle as it propagates through the porous material is the summation of the projectile bow shock wave strength and the very rapid nearly-isochoric deceleration of the material to equilibrium with the fragment given by

$$F_H = \frac{1}{2}\frac{s+1}{s}\rho_0 U^2 A, \tag{1}$$

where the linear approximation to the shock wave and particle velocity is used and ρ_0 and A are the the initial density of the porous material and the projected area of the bow shock wave, respectively [7]. In addition to this hydrodynamic force, there is an additional mechanical force, F_M, experienced by the propagating material that is associated with the work to deform the tile given approximately by

$$F_M = Y_0\, A, \tag{2}$$

where Y_0 is the crush strength of the porous material which is assumed here to be 0.8 and 35 MPa for the tile and TUFI/RCG, respectively. With these two retarding forces, the deceleration of the impacting particle remnants which are at rest with the shock wave compressed material is given by

$$\frac{1}{2}\frac{M}{s}\frac{dU^2}{dx} = -\left(\frac{1}{2}\frac{s+1}{s}\rho_0 U^2 + Y_0\right)A, \tag{3}$$

where M is the mass of the impacting particle and the swept mass.

To understand the differences between this work and the work previously reported by Christiansen, et al. in [4], especially when considering impacts at higher velocities and with sufficient high density sacrificial layers, it is necessary to consider the decomposition of waves within the target material to understand the cavity formation. In Figure 6a, a simple outline of an impact on the high density layer on the tile is shown. The projectile and high density layer being initially at zero pressure interacts and the projectile decelerates to the center of mass velocity of the equilibrium state for the two materials. Upon passage of the projectile through the high density layer to the low density tile it accelerates to the equilibrium state in the tile. This series of accelerations is easily seen in the shock wave pressure versus particle velocity plane for the three principal materials in the tile impacts (Figure 6b). The blue and the red curves represent the loci of shock wave states for the TUFI/RCG and the porous tile material, respectively, and are derived from SESAME 7360 for quartz, which is the principal component of these thermal protection tiles. The black curve is the loci of shock wave states for an aluminum projectile as derived from SESAME 3700. In this plane, each point of intersection represents a set of waves that conserve mass and momentum at an interface. For an aluminum projectile impacting a TUFI/RCG coated tile at a relative velocity of 9 km/s, the two waves that counter-propagate are shock waves at the pressure and particle velocity represented by the

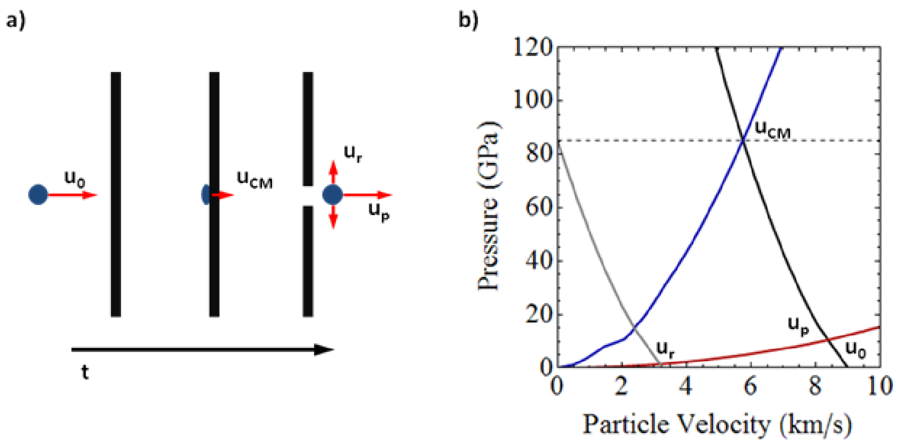

Figure 6. (a) Projectile reaction with high density layer and (b) wave decomposition of impact.

intersection of the blue and black curves. The shock wave velocities for the two waves are the slopes from the origin of the curve to the shock wave compressed state divided by the initial density of the material.

The shock wave in the projectile sets the adiabat for the subsequent release of the projectile material into the low-density tile material, which is a continuous process. The rarefaction wave in this plane is reasonably well approximated by the loci of shock wave states for the material, and as such, these states are all that are shown in this illustration. The resulting wave balance between the rarefaction wave in the projectile and the shock wave propagating in the tile is then the intersection of the aluminum release and the shock wave states of the tile. As can be seen in the figure, the projectile accelerates as it drops in pressure to near its initial impact velocity. Again, the shock wave velocity is merely the slope of the line originating from the origin for the tile to the balanced wave state divided by the initial density of the material. As the rarefaction wave propagating into the projectile reaches the vacuum interface, the projectile decompresses resulting in a decaying shock wave that eventually goes to sufficiently low strength so that the tile material strength is sufficient to stop the projectile material.

If the material is vaporized or fragmented to sufficiently small sizes to be eroded quickly, the material can also release radially from the impact direction. In Fig. 6b, this is represented by the gray curve which is at the pressure set by the interaction of the projectile and the TUFI/RCG layer but has no velocity relative to the surrounding medium in this direction. The shock wave compressed projectile decompresses along a rarefaction wave where the loci of shock wave states are again used to represent the available states. Like the waves in the propagation direction, the equilibrium shock wave with the surrounding porous material is achieved at the intersection with the shock wave states in the porous medium (red curve). In Fig. 7 the dependence of the ratio of the lateral release velocity of the projectile to the axial shock wave velocity is shown for TUFI/RCG layers that have an effective density of 1.6 g/cm^3 through 2.5 g/cm^3 in 0.3 g/cm^3 increments as derived from SESAME 3700 and 7360. It can be seen that this ratio approaches an asymptotic value of a half at high velocities and approaches more quickly the higher the effective density of the TUFI/RCG layer. As can be seen in this curve, the most significant variation is at low impact velocities and as the impact velocity increases the dependence becomes nearly constant at just below a half which would correspond to the asymptotic expansion into vacuum. Due to the isotropic nature of the porous tile, this relationship between lateral release and forward shock wave velocities leave a residual evidence in the impacted article as the ratio of half the width of the cavity diameter to penetration depth, respectively. In Fig. 8 the dependence of the ratio of half the width of the cavity to the penetration depth for the experimental records is shown as a function of the ratio of the effective projectile areal density to TUFI/RCG areal density. In this figure the cavity parameters are color sorted for based upon impact velocity with cyan, red, green, blue and purple representing 4, 7, 8, 9 and 9.5 km/s, respectively. The curves shown are fits to the data using a Fermi distribution function with the form

$$\omega = \frac{0.3}{Exp\left[\frac{\overline{m_P}\,U_m - \overline{m_T}\,U_i}{1/2\,\overline{m_T}\,U_m}\right] + 1} + 0.2, \qquad (4)$$

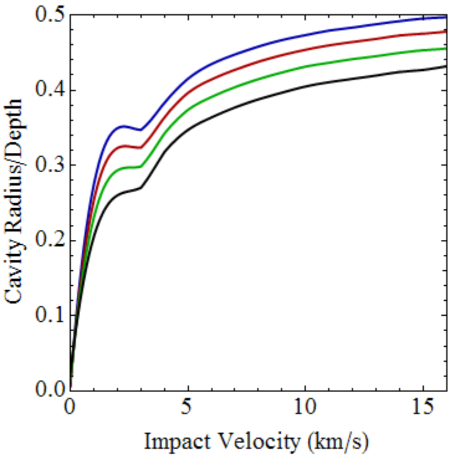

Figure 8. Dependence of the ratio of lateral release to axial shock wave velocity on impact velocity for 1.6 (black), 1.9 (green), 2.2 (red) and 2.5 g/cm^3 (blue)

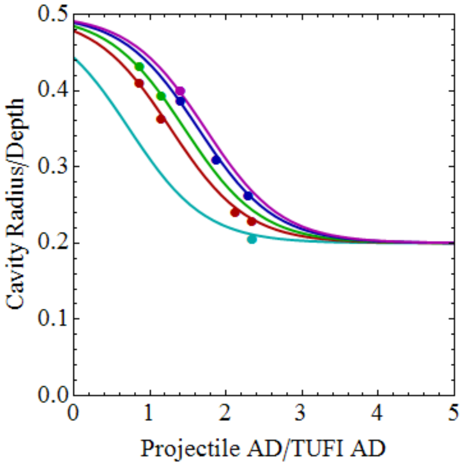

Figure 7. Cavity radius to penetration depth ratio as a function of projectile to TUFI/RCG areal density ratio

where $\overline{m_p}$ and $\overline{m_T}$ are the areal densities of the spherical projectile approximated as a cylinder and the TUFI/RCG layer, respectively, and U_i and U_m are the impact velocity and a fit factor for this data set of 5.5 km/s, respectively. It is also noted that the fit in this figure at high ratios of projectile to TUFI/RCG areal densities indicates a constant ratio of cavity radius to penetration depth. In this regime the TUFI/RCG layer is insufficient to breakup the projectile, so the projectile remains largely intact and cavity expansion is due to the compressed tile material itself releasing to the side. This can be again visualized in the shock wave pressure versus particle velocity plane (Figure 9a). The blue, red and black curves are as they are in Fig. 6b. The light blue curve represents the lateral release of the shock wave compressed tile material and the intersection of this curve and the red curve representing the attainable shock wave states in the uncompressed tile is the minimum ratio of release velocity to front velocity. The value of this minimum ratio of release velocity ot front velocity is shown in Figure 9b. As can be seen in this figure that this interpretation does lead to a nearly constant value independent of velocity and TUFI/RCG and projectile properties.

With the dependence of the radial shock wave velocity on the axial shock wave velocity, it is possible to modify Eqn. (4) to an effective expanding cylinder of radius $r = \omega\, x + r_p$, where ω and r_p are the slope of radial to axial shock wave velocities and the initial radius of the impacting projectile, respectively. Eqn. (4) on a per unit area basis of the effective cylinder then becomes

$$\frac{1}{s}\left(\frac{\overline{m_p}/\rho_0}{\left(1+\omega\, x/r_p\right)^2}+\frac{x}{3}\right)\frac{dU^2/U_0{}^2}{dx} = -\left(\frac{s+1}{s}\,\frac{U^2}{U_0{}^2}+\frac{Y_0}{1/2\,\rho_0\,U_0{}^2}\right), \qquad (5)$$

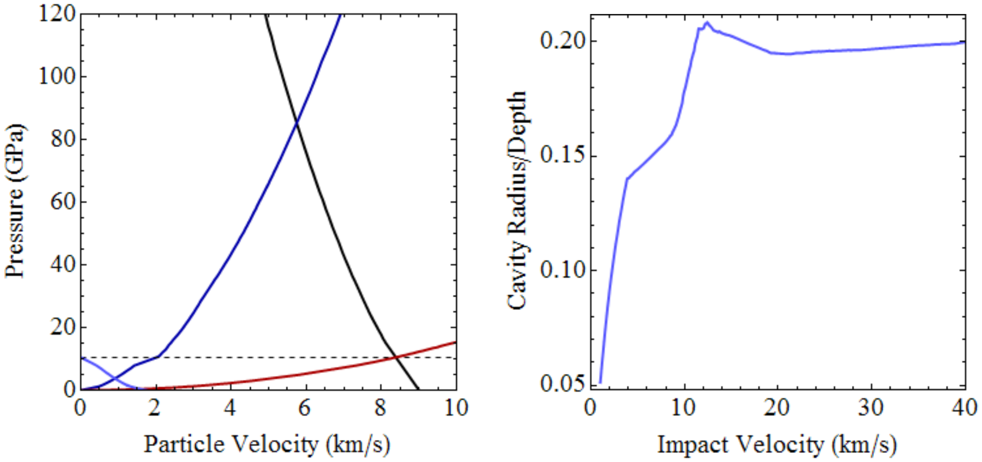

Figure 9. (a) Minimum cavity wave development and (b) ratio dependence on impact velocity.

where $\overline{m_p}$ is the areal density of the projectile prior to impact and TUFI/RCG layer, $\overline{m_T}$, given by $\overline{m_p} = (4/3)\, r_p\, \rho_p + \overline{m_T}$ and the one-third in the accreted mass term is due to the conical nature of the expansion. Additionally, Eqn. (5) is normalized to the initial velocity, U_0, of projectile as it breaks through the TUFI/RCG layer into the low density tile. This velocity is easily found from Eqn. (5) when the TUFI/RCG layer is treated as a delta function layer with shock wave compressed states on an isochor at the crystalline density with a relationship between shock wave and particle velocity with a slope s_T. The initial velocity's dependence on impact is

$$U_0 = U_i \left(\frac{\overline{m_p}}{\overline{m_p}+\overline{m_T}}\right)^{\frac{1+s_T}{2}}. \tag{6}$$

The full solution to Eqn. (8) is shown in Figure 10 in black for HITF-8313. In addition to the full solution, the asymptotic solution for small displacement and large displacement are shown in red and blue, respectively. The asymptotic solution for small displacement is

$$\frac{U^2}{{U_0}^2} \approx 1 - (s+1)\,\frac{\rho_0\, x}{\overline{m_p}}, \tag{7}$$

and the asymptotic solution for large displacement is

$$\frac{U^2}{{U_0}^2} \approx \left(\frac{2}{3}\frac{\omega\, \rho_p}{(s+1)\,\rho_0}\right)^{3s+3} \left(\frac{1}{2} + s\left(\frac{1}{2} + \frac{Y_0}{1/2\,\rho_0\,{U_0}^2}\right)\right) - \left(\frac{\omega\, x}{r_p}\right)^{3s+3} \frac{s\, Y_0}{1/2\,\rho_0\,{U_0}^2}, \tag{8}$$

Setting Eqn. (8) equal to zero and solving for the position x yields the final penetration depth given by

$$x_f \propto \frac{\rho_p\, r_p}{{\rho_0}^{5/6}} \frac{{U_i}^{1/3}}{{Y_0}^{1/6}} \left(\frac{\rho_p\, r_p}{\rho_p\, r_p + \overline{m_T}}\right)^{1/3}, \tag{9}$$

where s and s_T are taken to be approximately 1. For the case that the projectile is more significant than the TUFI/RCG layer, the relation for critical mass on penetrated depth into the tile becomes

$$m_c \propto \frac{{\rho_0}^{5/2}\, {x_f}^3\, {Y_0}^{1/2}}{{\rho_p}^2\, U_i}. \tag{10}$$

While these asymptotic solutions show how a weaker dependence of critical particle size on velocity is possible for this class of materials in a global sense, the quality of the model is not clear here. Using numerical integration methods, the full solution for the normal impact aluminum projectiles are calculated using Eqn. (4), (5) and (6) and

Table 2. Model comparison to normal impact Al data.

HITF #	*Measured (cm)*	*Calculated (cm)*
7468	1.10	1.20
9234	1.45	1.35
8297	1.10	1.20
9252	1.40	1.35
9313	2.50	2.35
9308	2.75	2.60
8313	2.20	2.20
9271	2.80*	2.80
9235	3.40	3.55
7469	3.85*	4.00
9314	4.40	4.50

* Equivalent penetration depth due to penetration into the densification layer

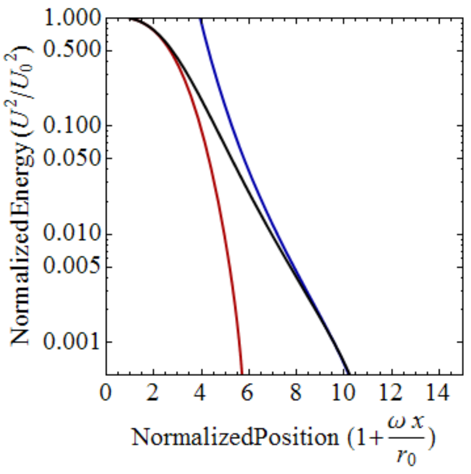

Figure 10. Normalized critical mass as a function of velocity for normal aluminum impacts

shown in Table 2.Model comparison to normal impact Al data.Table 2. The table includes the HITF test number for reference and the measured penetration compared with the calculated penetration. As can be seen this model reproduced the experimental findings to within 1.5 mm or less than 10% error.

The model predicted ballistic limit equation for a 3.81 cm tile with the 0.209 g/cm^2 TUFI/RCG coating is shown in Figure 11 in blue along with the ballistic limit equations for equal weight tiles with 0.158 g/cm^2 (green) and 0.044 g/cm^2 (red) tiles. In all three cases, projectiles below the respective curves are not expected to fully penetrate the tile

while projectiles above the curve are expected to fully penetrate the tile. The heavyweight TUFI/RCG tile is consistently better than the other TUFI/RCG coating weights. The model also demonstrates an analytical description to the long observed fragmentation and melt regime. Due to the higher apparent density of the heavyweight TUFI/RCG this fragmentation and melt regime is achieved at lower initial impact velocities than when lightweight TUFI/RCG and straight RCG layers are used.

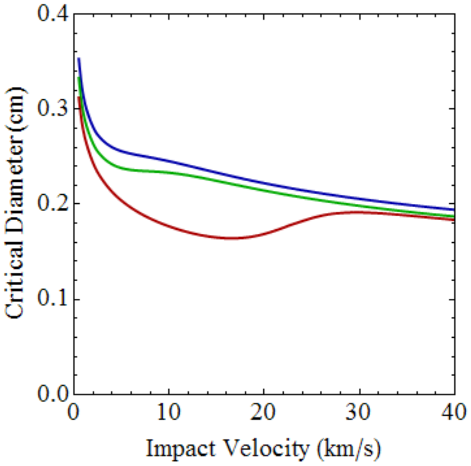

Figure 11. Ballistic limit curves for a 3.81 cm tile with heavyweight TUFI (blue) and equal weight tiles with lightweight TUFI (green) and RCG only (red) surface coatings

As has been shown in this model the shock wave compression is an important parameter to the ultimate ballistic performance of the tile. In previous work on silica aerogels it has been shown that the shock wave compression is changes constant values once very high shock wave strengths are achieved like the dependence shown in Figure 12 for 0.2 g/cm^3 silica aerogel from Boehly, *et al*. In this figure it can be seen that at shock wave strengths around ~10 GPa, the low density silicates become resistant to compression. This behavior has been attributed to the processes of dissociation and ionization taking place within the material at these high pressures resulting in an energy sink. This energy sink results in substantial mechanical work going into these material changes. This behavior has been incorporated in the model for the ballistic limit equations shown in Figure 13. Again these ballistic limit curves are shown for a 3.81 cm tile with a heavyweight TUFI/RCG coating in blue and equal weight tiles with lightweight TUFI/RCG coatings and just RCG coatings. In this case the onset of the limited compressibility of the tile material is achieved sooner for the plain RCG coating than the TUFI/RCG coatings. This is due to the greatly reduced velocity experienced by the projectile as it passes through the TUFI/RCG coatings resulting in lower shock wave strengths within the porous tiles. As such existing facilities are not expected to be able to show this behavior with the TUFI/RCG coated tiles, but may be able to demonstrate this behavior with a strictly RCG coated tile.

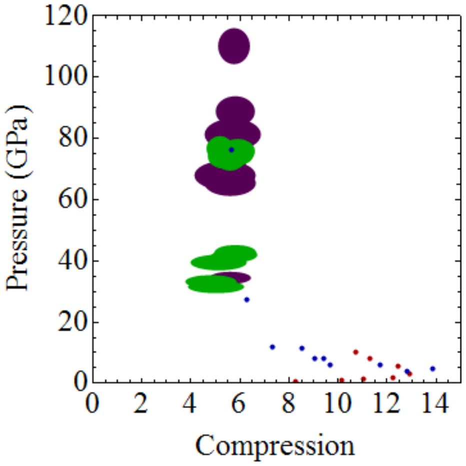

Figure 12. Pressure dependence on compression for 0.2 g/cm^3 silica red (Simakov/Trunin), blue (Vildanov), green (Knudson) and purple (Boehly).

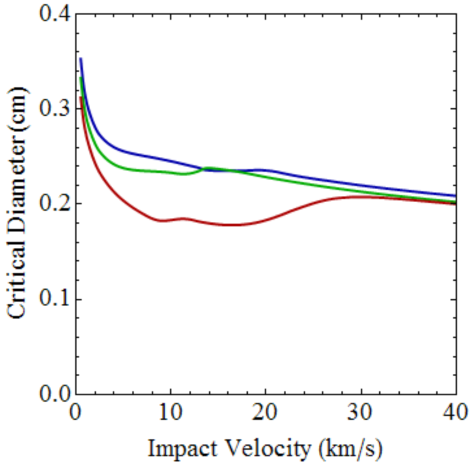

Figure 13. Ballistic limit curves for a 1.5” tile with heavyweight TUFI (blue), lightweight (green) and RCG only (red) surface coatings considering a variable *s* relationship

IV. Risk Assessment

To ascertain the impact of these observations, a cubic spacecraft model shown in Figure 14 has been run with the meteoroid and orbital debris environments experienced at the International Space Station to show how many penetrations are expected to occur with the model shown in Figure 4 relative to the ballistic limit equation reported by Christiansen, *et al*. The findings of this work is shown in Table 3. The environments used here are from the MEMCxPv2 model (#) and ORDEM2000 (#) model at an altitude of 400 kilometers and an inclination angle of 51.6°. The Bumper II (#) analysis program is used to combine the surface geometry, the environments and the shield performance defined here in comparison to that described in [4] to determine the probabilistic number of critical penetrations.

The configuration used for the shield performance in this analysis is representative of some of the configurations shown in Table 1. A total tile thickness of 3.55 cm with a density of 0.135 g/cm^3 along with a densification pickup from the TUFI/RCG layer of 0.209 g/cm^2 is used here. For aluminum particles representing orbital debris impacting at a velocity of 7 km/s, the shield performance from Fig. 3 predicts the configuration can protect against a 1.2 mm particle impacting normal to the surface or a 1.5 mm particle impacting at 45° to the surface normal. For nylon particles impacting at a velocity of 7 km/s, the BLE predicts the configuration can protect against a 1.9 mm particle impacting normal to the surface or a 2.4 mm particle impacting at 45° to the surface normal.

Each surface of the cube is set to the same configuration; however, the number of penetrations on each surface differed due to the directionality and velocity dependence of the environments. The environments are for a one year timeframe beginning at the year 2015. The percent decrease, change in critical penetrations from the shield performance described here to that in [4], is outlined in Table 3. This table shows this change for both orbital debris and meteoroids as a function of cube face. The overall decrease in critical penetrations due to both environments is about a 45%. The meteoroid component shows an about 80% decrease in risk; whereas, the orbital debris component remains approximately neutral. The shield performance described here is more penetrating for low velocities (<5 km/s) than that in the model described in [4], but higher velocity particles are less penetrating in this model. The positive percentages in Table 2 are reflections of this finding. For example, orbital debris strikes on the wake facing surface for orbital debris indicates the risk has gotten worse when using the shield performance outlined here because the relative velocity of the particles impacting on the wake face are reduced by the local orbital velocity of the cube; however, as the flux through the wake surface is much less than other surfaces, this increased number of critical penetrations is balanced by the decreased number of critical penetrations on other surfaces. In contrast, the wake face for meteoroids is relatively unaffected due to the fact that meteoroids are in a solar orbit rather than an Earth orbit. Due to the increased shield performance and the strong meteoroid population dependence on size, the predicted risk of a critical meteoroid impact is approximately five times less using the shield performance on TUFI/RCG coated tiles reported here as opposed to the extrapolation of shield performance derived from the non-TUFI/RCG coated tiles in [4].

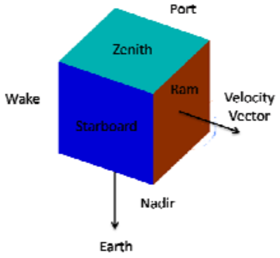

Figure 14. Cube model at ISS orbital parameters with principal vectors

Table 3. Penetration comparison to Christiansen, *et al.*

Cube Face	OD Diff (%)	MM Diff (%)
Ram	-50	-83
Wake	857	-82
Port	-42	-82
Stbd	-41	-82
Zenith	0	-82
Nadir	0	0

V. Conclusion

The advancement in test facilities to expand the velocity range available to hypervelocity impact studies with verifiable and repeatable projectiles has been leveraged to help reformulate the shield performance of thermal protection tiles. These studies have been with a varied set of tile properties, projectile material, impact velocities, impact angles and projectile sizes. Using a subset of this dataset, a model using the material equation of state tables and strength properties for tiles is derived here that explains these findings and facilitates the further extrapolation to alternative tile configurations and impact conditions. Further work is necessary to extend the model to oblique impacts and different projectile materials, along with, further testing and work is necessary to extend the model to alternative shapes of projectiles. Using the experimentally determined shield performance the overall risk to this material at ISS would be about neutral for orbital debris but would experience an approximate five-fold decrease in risk due to meteoroids.

Appendix

An appendix, if needed, should appear before the acknowledgements.

Acknowledgments

The preferred spelling of the word “acknowledgment” in American English is without the “e” after the “g.” Avoid expressions such as “One of us (S.B.A.) would like to thank…” Instead, write “F. A. Author thanks…” *Sponsor and financial support acknowledgments are also to be listed in the “acknowledgments” section.*

References

The following pages are intended to provide examples of the different reference types, as used in the AIAA Style Guide. When using the Word version of this template to enter references, select the “references” style from the drop-down style menu to automatically format your references. If you are using a print or PDF version of this document, all references should be in 9-point font, with reference numbers inserted in superscript immediately before the corresponding reference. You are not required to indicate the type of reference; different types are shown here for illustrative purposes only.

Periodicals

[1] Vatistas, G. H., Lin, S., and Kwok, C. K., “Reverse Flow Radius in Vortex Chambers,” *AIAA Journal*, Vol. 24, No. 11, 1986, pp. 1872, 1873.

[2] Dornheim, M. A., “Planetary Flight Surge Faces Budget Realities,” *Aviation Week and Space Technology*, Vol. 145, No. 24, 9 Dec. 1996, pp. 44-46.

[3] Terster, W., “NASA Considers Switch to Delta 2,” *Space News*, Vol. 8, No. 2, 13-19 Jan. 1997, pp., 1, 18.

All of the preceding information is required. The journal issue number (“No. 11” in Ref. 1) is preferred, but the month (Nov.) can be substituted if the issue number is not available. Use the complete date for daily and weekly publications. Transactions follow the same style as other journals; if punctuation is necessary, use a colon to separate the transactions title from the journal title.

Books

[4] Peyret, R., and Taylor, T. D., *Computational Methods in Fluid Flow*, 2nd ed., Springer-Verlag, New York, 1983, Chaps. 7, 14.

[5] Oates, G. C. (ed.), *Aerothermodynamics of Gas Turbine and Rocket Propulsion*, AIAA Education Series, AIAA, New York, 1984, pp. 19, 136.

[6] Volpe, R., “Techniques for Collision Prevention, Impact Stability, and Force Control by Space Manipulators,” *Teleoperation and Robotics in Space*, edited by S. B. Skaar and C. F. Ruoff, Progress in Astronautics and Aeronautics, AIAA, Washington, DC, 1994, pp. 175-212.

Publisher, place, and date of publication are required for all books. No state or country is required for major cities: New York, London, Moscow, etc. A differentiation must always be made between Cambridge, MA, and Cambridge, England, UK. Note that series titles are in roman type.

Proceedings

[7] Thompson, C. M., “Spacecraft Thermal Control, Design, and Operation,” *AIAA Guidance, Navigation, and Control Conference*, CP849, Vol. 1, AIAA, Washington, DC, 1989, pp. 103-115

[8] Chi, Y., (ed.), *Fluid Mechanics Proceedings*, SP-255, NASA, 1993.

[9] Morris, J. D. “Convective Heat Transfer in Radially Rotating Ducts,” *Proceedings of the Annual Heat Transfer Conference*, edited by B. Corbell, Vol. 1, Inst. Of Mechanical Engineering, New York, 1992, pp. 227-234.

At a minimum, proceedings must have the same information as other book references: paper (chapter) and volume title, name and location of publisher, editor (if applicable), and pages or chapters cited. Do not include paper numbers in proceedings references, and delete the conference location so that it is not confused with the publisher’s location (which is mandatory, except for government agencies). Frequently, CP or SP numbers (Conference Proceedings or Symposium Proceedings numbers) are also given. These elements are not necessary, but when provided, their places should be as shown in the preceding examples.

Reports, Theses, and Individual Papers

[10] Chapman, G. T., and Tobak, M., “Nonlinear Problems in Flight Dynamics,” NASA TM-85940, 1984.

[11] Steger, J. L., Jr., Nietubicz, C. J., and Heavey, J. E., “A General Curvilinear Grid Generation Program for Projectile Configurations,” U.S. Army Ballistic Research Lab., Rept. ARBRL-MR03142, Aberdeen Proving Ground, MD, Oct. 1981.

[12] Tseng, K., “Nonlinear Green’s Function Method for Transonic Potential Flow,” Ph.D. Dissertation, Aeronautics and Astronautics Dept., Boston Univ., Cambridge, MA, 1983.

Government agency reports do not require locations. For reports such as NASA TM-85940, neither insert nor delete dashes; leave them as provided by the author. Place of publication *should* be given, although it is not mandatory, for military and company reports. Always include a city and state for universities. Papers need only the name of the sponsor; neither the sponsor’s location nor the conference name and location are required. *Do not confuse proceedings references with conference papers*.

Electronic Publications

CD-ROM publications and regularly issued, dated electronic journals are permitted as references. Archived data sets also may be referenced as long as the material is openly accessible and the repository is committed to archiving the data indefinitely. References to electronic data available only from personal Web sites or commercial, academic, or government ones where there is no commitment to archiving the data are not permitted (see Private Communications and Web sites).

[13] Richard, J. C., and Fralick, G. C., “Use of Drag Probe in Supersonic Flow,” *AIAA Meeting Papers on Disc* [CD-ROM], Vol. 1, No. 2, AIAA, Reston, VA, 1996.

[14] Atkins, C. P., and Scantelbury, J. D., “The Activity Coefficient of Sodium Chloride in a Simulated Pore Solution Environment,” *Journal of Corrosion Science and Engineering* [online journal], Vol. 1, No. 1, Paper 2, URL: http://www.cp/umist.ac.uk/JCSE/vol1/vol1.html [cited 13 April 1998].

[15] Vickers, A., “10-110 mm/hr Hypodermic Gravity Design A,” *Rainfall Simulation Database* [online database], URL: http://www.geog.le.ac.uk/bgrg/lab.htm [cited 15 March 1998].

Always include the citation date for online references. Break Web site addresses after punctuation, and do not hyphenate at line breaks.

Computer Software

[16] TAPP, Thermochemical and Physical Properties, Software Package, Ver. 1.0, E. S. Microware, Hamilton, OH, 1992.

Include a version number and the company name and location of software packages.

Patents

Patents appear infrequently. Be sure to include the patent number and date.

[17] Scherrer, R., Overholster, D., and Watson, K., Lockheed Corp., Burbank, CA, U.S. Patent Application for a “Vehicle,” Docket No. P-01-1532, filed 11 Feb. 1979.

Private Communications and Web Sites

References to private communications and personal Web site addresses are generally not permitted. Private communications can be defined as privately held unpublished letters or notes or conversations between an author and one or more individuals. They *may* be cited as references in some case studies, but only with permission of the AIAA staff. Depending on the circumstances, private communications and Web site addresses may be incorporated into the main text of a manuscript or may appear in footnotes.

Unpublished Papers and Books

Unpublished works can be used as references as long as they are being considered for publication or can be located by the reader (such as papers that are part of an archival collection). If a journal paper or a book is being considered for publication choose the format that reflects the status of the work (depending upon whether it has been accepted for publication):

[18] Doe, J., “Title of Paper,” Conference Name, Publisher’s name and location (submitted for publication)
[19] Doe, J., “Title of Paper,” *Name of Journal* (to be published).
[20] Doe, J., “Title of Chapter,” *Name of Book*, edited by… Publisher’s name and location (to be published).
[21] Doe, J., “Title of Work,” Name of Archive, Univ. (or organization) Name, City, State, Year (unpublished).

Unpublished works in an archive *must* include the name of the archive and the name and location of the university or other organization where the archive is held. Also include any cataloging information that may be provided. Always query for an update if a work is about to be published.